2024 IEEE International Conference on Robotics and Automation (ICRA 2024)
May 13-17, 2024. Yokohama, Japan

A three-dimensional compliant bowtie-shaped mechanical amplifier to magnify coaxial displacement in a confined space

Jintaek Im[1,*], Eunsil Jang[1,*], and Cheol Song[1†]

***Abstract*— This paper proposes a novel form of a three-dimensional coaxial bowtie-shaped mechanical amplifier. The proposed model incorporates a lever mechanism into the Sarrus linkage structure. It allows the target plate to move along one axis with amplified displacement in a parallel manner. The amplifier was assembled after machining the components using a computer numerical control machine. A flexible hinge was incorporated into the amplifier design for simplified fabrication and reduced friction in the actuation mechanism. Castigliano's theorem is used to build a mathematical model of the proposed mechanical amplifier, and the performance was validated through finite element analysis and prototype fabrication. We achieved the amplification ratio of $\times 8.44$, resulting in the axial displacement up to 86 μm. The demonstrated amplifier is expected to apply to compact microsurgical robots or biomedical imaging apparatus requiring coaxial displacement amplification in confined spaces.**

I. Introduction

The piezoelectric (PZT) actuator is a compact device that facilitates precise displacement control with a distinct operation principle from conventional motors utilizing typical coil-based mechanisms [1]. Due to a high precision and fast response time, the PZT actuator has been generally adopted in various fields, such as precision stages [2], handheld microsurgical robots [3–5], energy harvesters [6], and miniature imaging apparatus [7], [8]. Each PZT element typically generates an elastic strain of approximately 0.1 %, leading to nanometric-scale displacements [9]. However, the PZT stack actuator can produce a cumulative displacement [10]. Although the stacked PZT can generate an affordable displacement, it is still insufficient for the extended applications to biomedical micro-positioning [11] and compact imaging systems [12].

In addition to exploring methods to enhance the deformation of PZT actuators, there has been active research in developing mechanical amplifiers [13–15]. Regarding cost and efficiency, mechanical amplifiers hold a distinct advantage, as they can exponentially extend the displacement at the input port by several to even several dozen times solely through a structural characteristic, facilitating transmission to the output port. There are three representative types of displacement amplifiers: rhombus-, bridge-, and lever types. The rhombus-type displacement amplifier exhibits input and output displacements in orthogonal directions, enveloping the input port with a closed-loop mechanical structure [9], [10], [16]. The bridge-type mechanical amplifier also requires a closed-loop structure with input and output displacements oriented orthogonally, incorporating flexural hinges and rigid links to induce high deformation [17], [18]. These methods necessitate the orthogonal arrangement of the PZT stack for axial amplification, resulting in a considerably larger system dimension.

Conversely, the lever mechanism has the same direction as the input and output displacements by importing the fixed part, the input force part, and the output action part, enabling a substantial amplification ratio [8], [19–21]. Therefore, various studies have integrated lever mechanisms by incorporating them with different amplifier types. In particular, the hybrid mechanical amplifiers that combine the bridge type and the lever mechanism could obtain a coaxial amplification [22], [23] with a high amplification ratio of more than $\times 10$. However, they still possess relatively larger dimensions, limiting their applicability in confined spaces. Hence, additional research is essential for depth-scanning applications such as industrial [24], biological [25], or medical imaging [26], which demand axis-aligned amplification within limited system spaces. Furthermore, the compact mechanical amplifier could be integrated with robotic systems to apply force or induce subtle displacements in various applications, such as robotic palpation [27] and minimally invasive surgical robots [28], addressing challenges in narrow spaces and providing sufficient force and displacement in samples.

The contribution of this paper is to propose a novel type of bowtie-shaped displacement amplifier applicable to narrow diameters by combining the flexural hinge-based Sarrus linkage and lever mechanism to magnify coaxial displacement in a confined space. Sarrus linkage is a representative structure that makes rotational motion straight [29] and has been combined with compliant joints [30], finding various applications as multistable elastic structures. The presented displacement amplifier used four flexure hinges and applied lever mechanism to one of the hinges, amplifying the output displacement like a squat motion. It achieved coaxial amplification of $\times 8.44$ along the PZT's displacement. For the mathematical modeling, Castigliano's theorem[31], [32] was applied by dividing the analytical sections on the designed structure. It enabled the calculation of deflection at specific points within a mechanical structure using an energy-based principle, offering the advantages of simplicity in mathematical representation, high accuracy, and rapid computation. The transformation matrix between applied

† Corresponding author, * Equal contribution
[1]Department of Robotics and Mechatronics Engineering, DGIST, Daegu 42988, South Korea (wlsehd23,leun_1427, csong)@dgist.ac.kr

*This work was supported by the DGIST R&D Program of the Ministry of Science and ICT (23-RT-01) and the Technology Innovation Program funded by the Ministry of Trade, Industry & Energy(MOTIE, KOREA)(20023168).

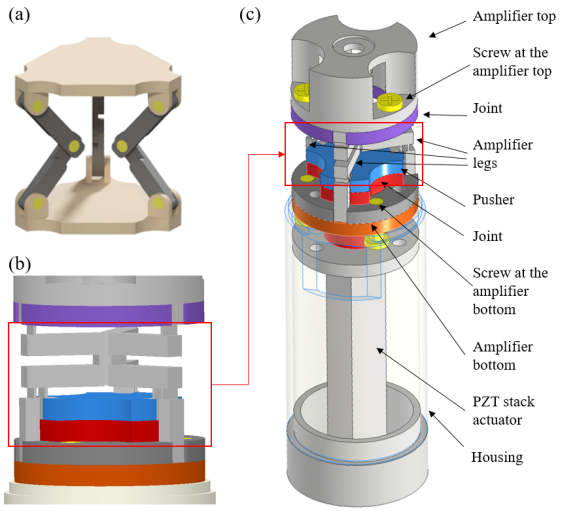

Fig. 1. (a) The conventional Sarrus linkage. (b) The proposed amplifier structure with the modified Sarrus linkage and lever mechanism. (c) The internal architecture.

forces and output displacement was derived, with further consideration given to the piezoelectric characteristics of an actuator. The performance of the implemented mechanical amplifier with its mathematical model was verified through finite element analysis (FEA), and prototype testing.

II. Materials and Methods

A. System Design

The basic structure of the Sarrus linkage is shown in Fig. 1(a), which can transform the circular motion of the lower link into linear motion, resembling the unfolding of bent legs. However, its constrained amplification ratio and dimensional requirements pose challenges for implementation in confined settings. The proposed bowtie-shaped mechanical amplifier is shown in Fig. 1(b), where we incorporate a lever mechanism onto the lower link of the Sarrus linkage. A structure was devised where a portion of the lower link is fixed, and it facilitates displacement amplification by transmitting the input displacement from the PZT actuator to the upper output displacement. To prevent three-dimensional torsion, we arranged three legs in triangular form, and flexure hinges were employed at the joints to mitigate energy loss due to friction.

The detailed architecture of the proposed bowtie-shaped mechanical amplifier is shown in Fig. 1(c). The amplifier top is the moving part, and the amplifier bottom includes three grooves to fix the three amplifier legs. The pusher transfers the input displacement of the PZT actuator to the amplifier legs, enabling the relative movement from the outer housing. Here, we utilized P-883.51 (dimensions: $3\ \mathrm{mm}\times3\ \mathrm{mm}\times18\ \mathrm{mm}$, PI Ceramic GmbH, Germany) as the stack PZT actuator, and the amplifier leg was crafted from Aluminum alloy through custom manufacturing using a computer numerical control (CNC) machine. The amplifier leg is crucial; one part is fixed to the outer housing by the amplifier bottom, and the other is set to the top. It has four

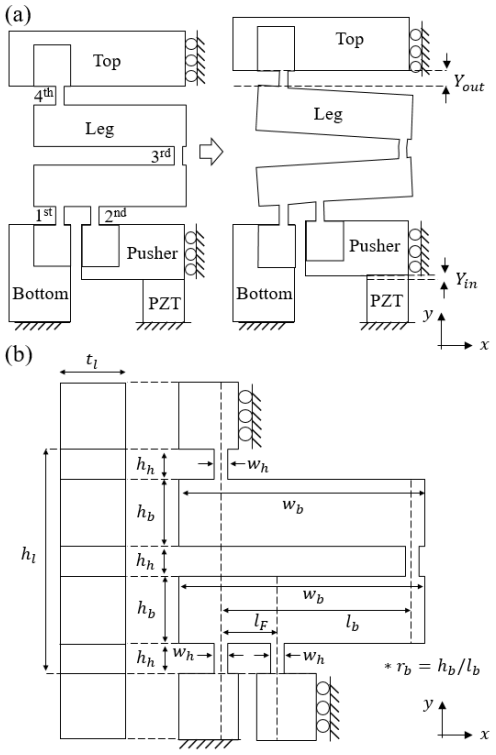

Fig. 2. (a) The schematic diagram of the deformation in the proposed mechanical amplifier. (b) The dimensions of the proposed mechanical amplifier

flexure hinges, which are symmetrically arranged to push the amplifier top parallel. The detailed mechanism of amplification will be elaborated in the next section. The housing is designed in a cylindrical shape with an outer diameter and length of $7\ \mathrm{mm}$ and $25\ \mathrm{mm}$, respectively. There are three screws each on the amplifier's top and bottom, ensuring a tight mechanical fixation with the amplifier legs. Due to tolerances introduced by manufacturing, there was a slight gap in the mechanical fixation, which was further reinforced by using epoxy resin to increase the bonding force.

B. Analytical Modeling

The schematic diagram of the deformed mechanical amplifier is shown in Fig. 2(a). The leg can be divided into four flexural hinges, two connecting beams, and three joints. The hinges attached to the amplifier's bottom and top are denoted as the first and fourth hinges, respectively. The hinge attached to the pusher is the second hinge, and the hinge connecting two beams is the third hinge. The input deformation (Y_{in}) is achieved by a PZT stack actuator. The structure of the proposed amplifier can provide the enlarged displacement output (Y_{out}) at the amplifier's top. Here, the bottom of the amplifier and PZT actuator are fixed, and the sides of the pusher and amplifier's top are regarded as rotation-fixed and translation-free surfaces.

The dimensions of the proposed amplifier leg are shown in Fig. 2(b). The left part shows the leg's cross-section, consisting of a uniform thickness, t_l. The width and height of a flexural hinge are denoted as w_h and h_h, respectively.

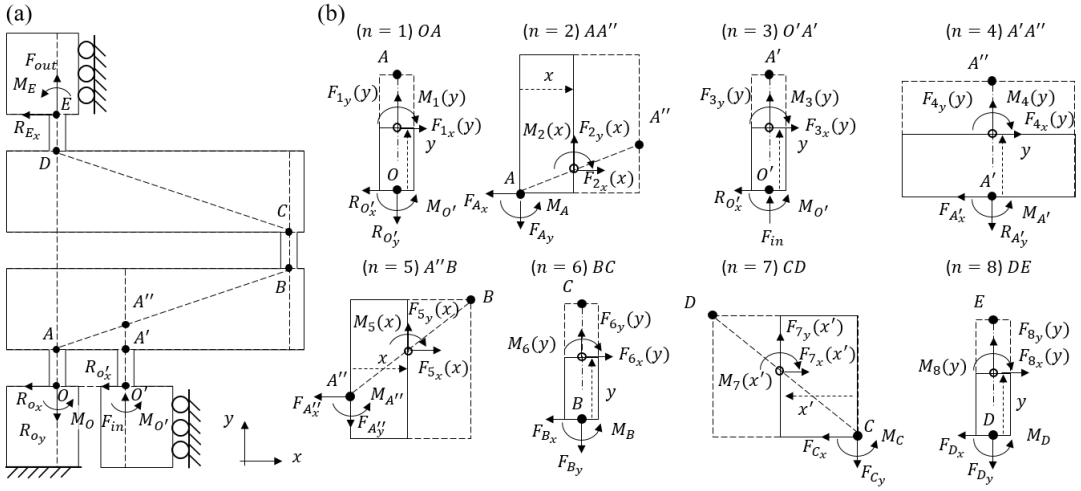

Fig. 3. The mathematical modeling of the proposed mechanical amplifier. The free-body diagrams of (a) the entire mechanism and (b) each analytical section are shown.

The width and height of a connecting beam are w_b and h_b, respectively. The ratio between h_b and l_b is denoted as r_b; $r_b = h_b/l_b$. The first and fourth hinges are vertically aligned. In addition, the second and third hinges have a horizontal offset from the first hinge of l_F and l_b, respectively. h_l is the height between the two joints attached to the amplifier's top and bottom, so it equals $3h_h + 2h_b$.

The free-body diagram of the proposed amplifier's leg is illustrated in Fig. 3(a). We set nine analytical coordinates; O, O', A, A', A'', B, C, D, and E, and two external loads of F_{in} and F_{out} are assumed to be applied along the y-axis. There exist four reaction loads, R_{O_x}, R_{O_y}, $R_{O'_x}$, and R_{E_x}, and three reaction moments of M_O, $M_{O'}$, and M_E, respectively. Based on the force and moment equilibrium, R_{O_x}, R_{O_y}, and M_O can be expressed as follows:

$$\begin{aligned} R_{O_x} &= -R_{O'_x} - R_{E_x} \\ R_{O_y} &= F_{in} + F_{out} \\ M_O &= -M_{O'} - M_E - R_{E_x} \cdot h_l - F_{in} \cdot l_F. \end{aligned} \tag{1}$$

For the calculation of the internal loads and moments, the free-body diagrams for each analytical section are shown in Fig. 3(b). In the section OA, the equilibrium analysis is performed along the y-axis at $0 \le y \le h_h$, resulting in the following equations:

$$\begin{aligned} F_{1_x}(y) &= -R_{O'_x} - R_{E_x} \\ F_{1_y}(y) &= F_{in} + F_{out} \\ M_1(y) &= -M_{O'} - M_E + R_{O'_x} \cdot y - R_{E_x} \cdot (h_l - y) - F_{in} \cdot l_F. \end{aligned} \tag{2}$$

In the section AA', the analysis is performed at $0 \le x \le l_F$, resulting in the following equations:

$$\begin{aligned} F_{2_x}(x) =& -R_{O'_x} - R_{E_x} \\ F_{2_y}(x) =& F_{in} + F_{out} \\ M_2(x) =& -M_{O'} - M_E + R_{O'_x} \cdot (h_h + r_b \cdot x) \\ & - R_{E_x} \cdot (h_l - h_h - r_b \cdot x) - F_{in} \cdot (l_F - x) + F_{out} \cdot x. \end{aligned} \tag{3}$$

In the section $O'A'$, the analysis range is $0 \le y \le h_h$:

$$\begin{aligned} F_{3_x}(y) =& R_{O'_x} \\ F_{3_y}(y) =& -F_{in} \\ M_3(y) =& M_{O'} - R_{O'_x} \cdot y. \end{aligned} \tag{4}$$

In the section $A'A''$, the analysis range is $0 \le y \le r_b l_F$:

$$\begin{aligned} F_{4_x}(y) =& R_{O'_x} \\ F_{4_y}(y) =& -F_{in} \\ M_4(y) =& M_{O'} - R_{O'_x} \cdot (h_h + y) \end{aligned} \tag{5}$$

where the force and moments from the two path, O and O', are combined at A''. In the section $A''B$, the analysis range is $0 \le x \le l_b - l_F$:

$$\begin{aligned} F_{5_x}(x) =& -R_{E_x} \\ F_{5_y}(x) =& F_{out} \\ M_5(x) =& -M_E - R_{E_x} \cdot (h_l - h_h - r_b \cdot (l_F + x)) \\ & + F_{out} \cdot (l_F + x) \end{aligned} \tag{6}$$

where coefficients for $R_{O'_x}$, F_{in}, and $M_{O'}$ are eliminated. In the section BC, the analysis range is $0 \le y \le h_h$:

$$\begin{aligned} F_{6_x}(y) =& -R_{E_x} \\ F_{6_y}(y) =& F_{out} \\ M_6(y) =& -M_E - R_{E_x} \cdot (h_l - h_h - h_b - y) + F_{out} \cdot l_b. \end{aligned} \tag{7}$$

In the section CD, the analysis is done to the opposite direction of x (x') at $0 \le x' \le l_b$:

$$\begin{aligned} F_{7_x}(x') =& -R_{E_x} \\ F_{7_y}(x') =& F_{out} \\ M_7(x') =& -M_E - R_{E_x} \cdot (h_l - 2h_h - h_b - r_b x') \\ & + F_{out} \cdot (l_b - x'). \end{aligned} \tag{8}$$

In the final section, DE, the analysis range is $0 \le y \le h_h$:

$$\begin{aligned} F_{8_x}(y) =& -R_{E_x} \\ F_{8_y}(y) =& F_{out} \\ M_8(y) =& -M_E - R_{E_x} \cdot (h_l - 2h_h - 2h_b - y). \end{aligned} \tag{9}$$

Based on Castigliano's second theorem[31], [32], the deflection of the mechanical system can be calculated by using strain energy. For the calculation of the strain energy, we have considered energies caused by bending moments, shear, and axial loads, resulting in Y_{in} and Y_{out} as follows:

$$\begin{aligned} Y_{in} &= \sum_{n=1}^{8} \int_0^{l_{s_n}} \left(\frac{M_n}{EI_n} \frac{\partial M_n}{\partial F_{in}} + \frac{F_{n_s}}{GA_n} \frac{\partial F_{n_s}}{\partial F_{in}} + \frac{F_{n_a}}{EA_n} \frac{\partial F_{n_a}}{\partial F_{in}} \right) ds_n \\ Y_{out} &= \sum_{n=1}^{8} \int_0^{l_{s_n}} \left(\frac{M_n}{EI_n} \frac{\partial M_n}{\partial F_{out}} + \frac{F_{n_s}}{GA_n} \frac{\partial F_{n_s}}{\partial F_{out}} + \frac{F_{n_a}}{EA_n} \frac{\partial F_{n_a}}{\partial F_{out}} \right) ds_n \end{aligned} \tag{10}$$

where n is a section number, and s_n is an n-th analytical axis with their lengths of l_{s_n}. F_{n_s} and F_{n_a} are the shear and axial forces at n-th section, respectively. E and G are Young's Modulus and Shear Modulus, respectively. As we used an aluminum alloy as a material, each value is 71.7 GPa and 26.9 GPa, respectively[31]. I_n and S_n are the second moment of area and cross-section area at n-th section, respectively. In section numbers of 1, 3, 6, and 8, $I_n = t_l h_h^3/12$ and $S_n = t_l h_h$ are used. In section numbers of 2, 5, and 7, $I_n = t_l h_b^3/12$ and $S_n = t_l h_b$ are used. For section number of 4, $I_n = t_l w_b^3/12$ and $S_n = t_l w_b$ are used. Hence, most of the deformation occurs in flexural hinges due to their relatively lower EI values. The result of (10) can be represented by a matrix form as follows:

$$\begin{bmatrix} Y_{in} \\ Y_{out} \end{bmatrix} = \begin{bmatrix} v_{11} & \dots & v_{16} \\ v_{21} & \dots & v_{26} \end{bmatrix} \begin{bmatrix} M_{O'} \\ M_E \\ R_{O'_x} \\ R_{E_x} \\ F_{in} \\ F_{out} \end{bmatrix} \tag{11}$$

where six independent variables exist; $M_{O'}$, M_E, $R_{O'_x}$, R_{E_x}, F_{in} and F_{out}. For our system, the F_{in} and F_{out} are the desired input parameters, thus four more complementary equations are required as follows:

$$\begin{aligned} \theta_{O'} &= \sum_{n=1}^{8} \int_0^{l_{s_n}} \frac{M_n}{EI_n} \frac{\partial M_n}{\partial M_{O'}} ds_n = 0 \\ \theta_E &= \sum_{n=1}^{8} \int_0^{l_{s_n}} \frac{M_n}{EI_n} \frac{\partial M_n}{\partial M_E} ds_n = 0 \\ X_{O'} &= \sum_{n=1}^{8} \int_0^{l_{s_n}} \left(\frac{M_n}{EI_n} \frac{\partial M_n}{\partial R_{O'_x}} + \frac{F_{n_s}}{GA_n} \frac{\partial F_{n_s}}{\partial R_{O'_x}} + \frac{F_{n_a}}{EA_n} \frac{\partial F_{n_a}}{\partial R_{O'_x}} \right) ds_n = 0 \\ X_E &= \sum_{n=1}^{8} \int_0^{l_{s_n}} \left(\frac{M_n}{EI_n} \frac{\partial M_n}{\partial R_{E_x}} + \frac{F_{n_s}}{GA_n} \frac{\partial F_{n_s}}{\partial R_{E_x}} + \frac{F_{n_a}}{EA_n} \frac{\partial F_{n_a}}{\partial R_{E_x}} \right) ds_n = 0 \end{aligned} \tag{12}$$

$$\begin{bmatrix} w_{11} & \dots & w_{16} \\ \vdots & \vdots & \vdots \\ w_{41} & \dots & w_{46} \end{bmatrix} \begin{bmatrix} M_{O'} \\ M_E \\ R_{O'_x} \\ R_{E_x} \\ F_{in} \\ F_{out} \end{bmatrix} = \begin{bmatrix} 0 \\ 0 \\ 0 \\ 0 \end{bmatrix}. \tag{13}$$

Based on (13), $M_{O'}$, M_E, $R_{O'_x}$, and R_{E_x} can be expressed by F_{in} and F_{out} as follows:

$$\begin{aligned} \begin{bmatrix} M_{O'} \\ M_E \\ R_{O'_x} \\ R_{E_x} \end{bmatrix} &= - \begin{bmatrix} w_{11} & \dots & w_{14} \\ \vdots & \vdots & \vdots \\ w_{41} & \dots & w_{44} \end{bmatrix}^{-1} \begin{bmatrix} w_{15} & w_{16} \\ \vdots & \vdots \\ w_{45} & w_{46} \end{bmatrix} \begin{bmatrix} F_{in} \\ F_{out} \end{bmatrix} \\ &= \begin{bmatrix} c_{11} & c_{12} \\ \vdots & \vdots \\ c_{41} & c_{42} \end{bmatrix} \begin{bmatrix} F_{in} \\ F_{out} \end{bmatrix}. \end{aligned} \tag{14}$$

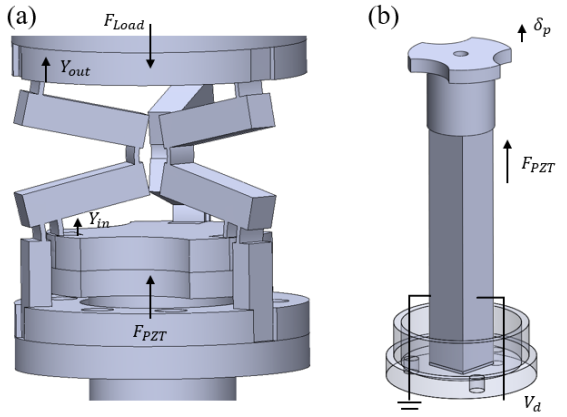

Fig. 4. (a) Schematic diagram of the deformed mechanical amplifier. (b) Parameters for the stacked PZT.

By using (11) and (14), the transformation matrix (T) between $[Y_{in}, Y_{out}]^T$ and $[F_{in}, F_{out}]^T$ can be derived as follows:

$$\begin{bmatrix} Y_{in} \\ Y_{out} \end{bmatrix} = T \begin{bmatrix} F_{in} \\ F_{out} \end{bmatrix} = \begin{bmatrix} T_{11} & T_{12} \\ T_{21} & T_{22} \end{bmatrix} \begin{bmatrix} F_{in} \\ F_{out} \end{bmatrix}$$

$$\begin{bmatrix} T_{11} & T_{12} \\ T_{21} & T_{22} \end{bmatrix} = \begin{bmatrix} v_{11} & \dots & v_{14} \\ v_{21} & \dots & v_{24} \end{bmatrix} \begin{bmatrix} c_{11} & c_{12} \\ \vdots & \vdots \\ c_{41} & c_{42} \end{bmatrix} + \begin{bmatrix} v_{15} & v_{16} \\ v_{25} & v_{26} \end{bmatrix}. \tag{15}$$

As (15) is derived in one amplifier's leg, it is necessary to expand the model for the proposed three legs configuration. The input force is generated by the stacked PZT at the bottom, F_{PZT}, and the external load, F_L is applied from the amplifier's top, as shown in Fig. 4(a). Due to the symmetricity, both F_{PZT} and F_L are assumed to be evenly distributed to three amplifier's legs; $F_{in} = \frac{1}{3} F_{PZT}$ and $F_{out} = -\frac{1}{3} F_L$. Hence, Y_{in} and Y_{out} can be expressed by F_{PZT} and F_L as follows:

$$\begin{bmatrix} Y_{in} \\ Y_{out} \end{bmatrix} = \frac{1}{3} \begin{bmatrix} T_{11} & -T_{12} \\ T_{21} & -T_{22} \end{bmatrix} \begin{bmatrix} F_{PZT} \\ F_L \end{bmatrix}. \tag{16}$$

The stacked PZT exerts both force and displacement by the applied driving voltage, V_d, as shown in Fig. 4(b). Based on electromechanical properties of piezoelectric elements[33], F_{PZT} can be expressed as follows:

$$F_{PZT} = \frac{F_{block,max}}{V_{max}} V_d - \frac{F_{block,max}}{\delta_{free,max}} \delta_p = k_v V_d - k_\delta \delta_p \tag{17}$$

where $F_{block,max}$ is the maximum blocking force required to prevent the deflection of the PZT(δ_p), V_{max} is the highest admissible voltage, and $\delta_{free,max}$ is a maximum achievable deflection in the absence of external loading conditions. Here, δ_p equals to Y_{in}, thus, $[Y_{in}, Y_{out}]^T$ can be redefined by substituting F_{PZT} in (16) with (17) as follows:

$$\begin{bmatrix} Y_{in} \\ Y_{out} \end{bmatrix} = \begin{bmatrix} \frac{k_v T_{11}}{3+k_\delta T_{11}} & -\frac{T_{12}}{3+k_\delta T_{11}} \\ \frac{k_v T_{21}}{3+k_\delta T_{11}} & -\frac{\left(T_{22}+\frac{1}{3}k_\delta T_{11} T_{22} - \frac{1}{3} k_\delta T_{12} T_{21}\right)}{3+k_\delta T_{11}} \end{bmatrix} \begin{bmatrix} V_d \\ F_L \end{bmatrix}. \tag{18}$$

Thus, $[Y_{in}, Y_{out}]^T$ can be calculated by the input force generated by the actuator, (16), or by the driving voltage, (18).

C. Model Validation

For the calculation of T, we used MATLAB software. As all the integration procedures contain the same bending moments, shear forces, and axial forces, establishing a common integration function and changing only the partial derivative terms (e.g., $\partial M/\partial F$) can substantially simplify the calculation. As a finite-element analysis (FEA), we build a 3D model by SolidWorks and perform the static and modal analysis by ANSYS software. The mesh, comprising around 15,000 elements, is generated using adaptive sizing, with the smallest element size set to 80 μm. Static Structural Analysis is employed to calculate elastic deformation, while Harmonic Analysis is used to determine resonant frequencies.

TABLE I
STRUCTURAL PARAMETERS

Name	Value (mm)	Name	Value (mm)
w_h	0.15	h_l	3.50
h_h	0.50	t_l	1.00
w_b	3.80	l_F	0.55
h_b	1.00	l_b	3.25

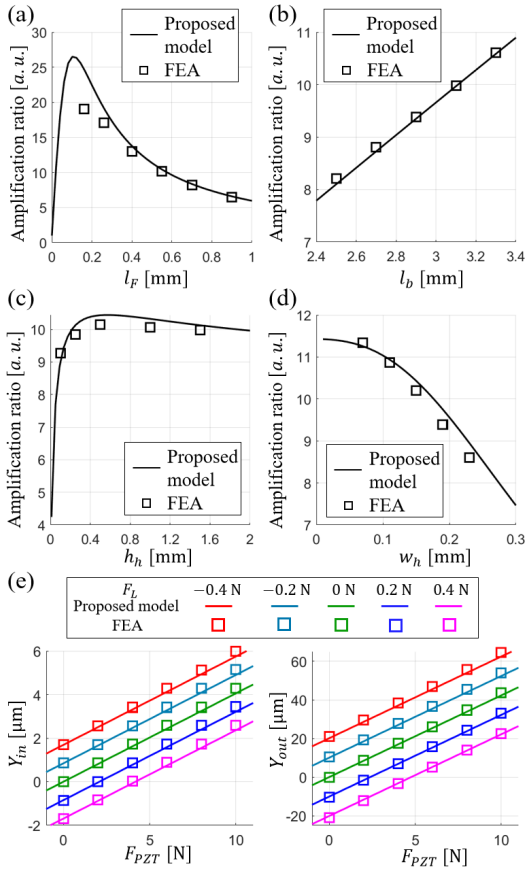

Fig. 5. Comparison between the proposed model and FEA results in varying geometrical parameters. (a) l_F variant. (b) l_b variant. (c) h_h variant. (d) w_h variant.(e) Effects of F_{PZT} and F_L on Y_{in} and Y_{out}

The structural parameters are listed in Table 1. Among the parameters, l_F and l_b are related to the lever mechanism, and w_h and h_h correspond to the elastic deformation of the flexural hinge, respectively. We regarded these four parameters as the most influential variables. The analysis results on the amplification ratio (Y_{out}/Y_{in}) by the proposed model and FEA are compared, as shown in Figs. 5(a) to (d). For each variant case, other parameters are set to the original values listed in Table 1.

For the l_F variant case (Fig. 5(a)), the proposed model and FEA have a good agreement, showing a main difference near the peak. Ignoring higher-order elastic deformations and relying on the typical assumption of constant and linear moment calculations for flexure hinges might have introduced significant errors near the lever peak [34]. However, amplifier structures are typically determined away from the lever peak to prevent excessive stress on the flexure hinge. Therefore, our model produced satisfactory results, especially when l_F exceeds 0.5 mm.

For the l_b variant case (Fig. 5(b)), the proposed model and FEA results have a similar linear trend on the amplification ratio. The higher l_b is applied, the larger amplification ratio is achieved owing to the lever mechanism.

The result from the varying h_hs shows a similar trend with the l_F result (Fig. 5(a)) with a less dominant peak, as shown in Fig. 5(c). In addition, w_h also plays an essential role in the hinge deflection. The thicker the w_h, the less the amplification ratio, as shown in Fig. 5(d). Both h_h and w_h results by the proposed model have a good agreement with FEA results.

The comparison result of the static force response is shown in Fig. 5(e). The structural parameters listed in Table 1 are applied, and F_{PZT} from 0 N to 10 N with F_L from -0.4 N to 0.4 N are analyzed. Due to the lever structure, F_L affects the output displacement approximately ten times higher than F_{PZT}. Analysis results by the proposed model and FEA are well-fitted to each other, resulting in a prediction error of 2.5 ± 1.7 %. Moreover, the proposed model offers a computation time that is ∼200 times faster than the FEA. Specifically, the proposed model only necessitates approximately 0.09 s per case, whereas FEA consumes around 18 s.

We set the desired Y_{out} as 100 μm. Taking the inverse transformation matrix in (16) enables calculating the required PZT forces to achieve a certain value of Y_{out}. The input force of 20.9 N is required to maneuver the amplifier top to 100 μm without an external load, as shown in Fig. 6(a). In this case, a maximum stress of 308.88 MPa is applied to the third flexural hinge, as shown in Fig. 6(b). This value is designed to be less than the yield stress of an Aluminum, ∼500 MPa[31]. The modal analysis was also performed to preclude an involuntary resonance. The first resonance is found at 981.4 Hz in the y-direction, as shown in Fig. 6(c). The second resonance has a rotational vibration at 1546.1 Hz, as shown in Fig. 6(d). These resonant frequencies are sufficiently high regarding the typical speed of the depth imaging system. Thus, the proposed mechanical amplifier can provide enough depth-scanning range with a small force while avoiding resonance.

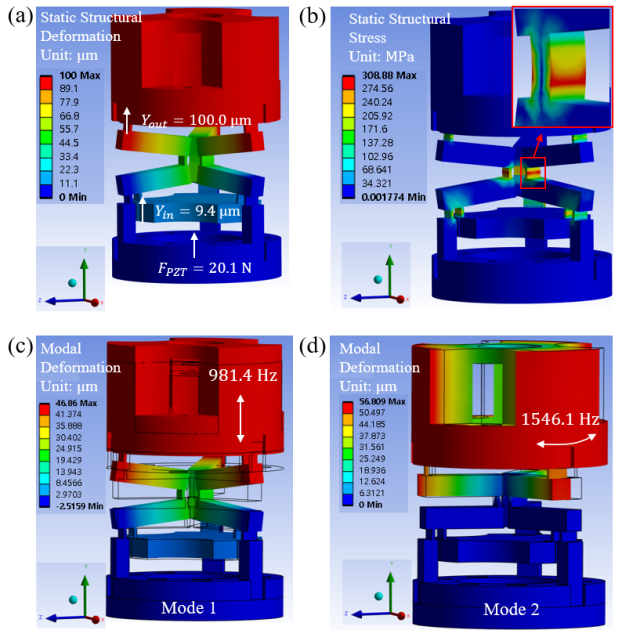

Fig. 6. FEA simulation results. (a) The displacement result of the deformed mechanical amplifier. (b) The stress analysis result. (c) and (d) Modal analysis results in the first mode and second mode, respectively.

III. Results and Discussion

Fig. 7(a) shows the implemented system and measurement setup. A one-channel PZT driver (E-413.OE, PI Ceramic GmbH, Germany) amplifies the input voltage by 50 times, and the PZT stack actuator is inserted inside the fabricated mechanical amplifier. For measuring displacement, a high-precision capacitive sensor (C8-3.2, Lion Precision, USA) and its driver (CPL190, Lion Precision, USA) are used, providing a measurement resolution and range of 3 nm and 0.5 mm, respectively. We used a data acquisition (DAQ) board (PCIe-6374, National Instrument, USA) and made custom software with Visual C++, operating at 1 kHz. The prototype mechanical amplifier is well-manufactured, having a handheld size (Φ =7 mm, L =25 mm) and weight (<4.8 g).

The structure of the implemented amplifier's leg is shown in Fig. 7(b). After applying a 100 V, it is readily noticeable that Y_{out} gets to have a much larger displacement than Y_{in}. We used sinusoidal input voltages ranging from 0 V to 100 V to analyze an amplification ratio. The representative displacement results of Y_{in} and Y_{out} are shown in Fig. 7(c). For the twenty repetitions of sawtooth waveforms, the hysteresis of Y_{in} and Y_{out} are analyzed, as shown in Fig. 7(d). We obtained an actual amplification ratio of $\times 8.44$, slightly smaller than the predicted values by the proposed model ($\times 10.4$) and the FEA ($\times 10.2$). The reduction of the amplifier would stem from the friction caused by the manufacturing tolerance and misalignment of each component. Despite this error, the implemented mechanical amplifier successfully achieved a displacement range of 86 µm, which is still $\times 5.73$ times larger than the maximum free deflection of the bare PZT stack.

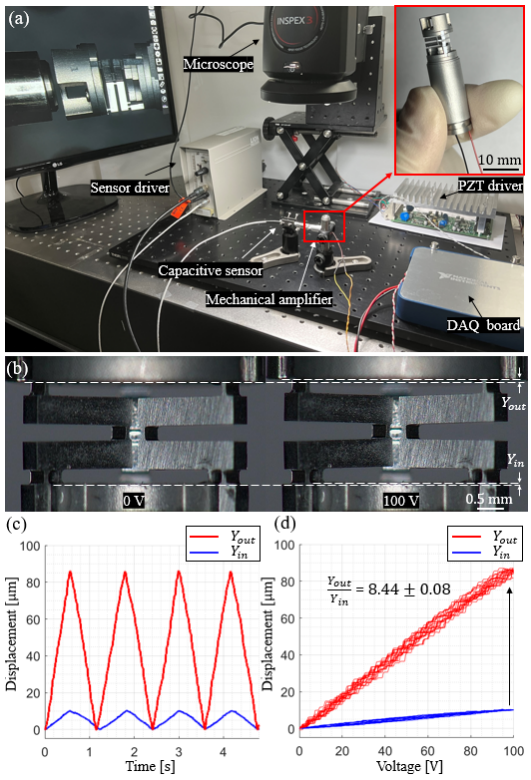

Fig. 7. Implementation of the mechanical amplifier. (a) Experimental setup. (b) Magnified images of the amplifier's leg before and after applying voltage. (c) Displacement results from a sawtooth input voltage. (d) Amplification results.

IV. Conclusion

This study proposed a compliant bowtie-shaped mechanical amplifier to enhance the coaxial displacement using a stacked PZT actuator and Sarrus linkage with a lever mechanism. Castigliano's theorem was applied to build a mathematical model for the kinematic analysis. The entire amplifier structure was divided into eight analytical sections, and each force and moment were derived. The proposed model showed a good agreement with FEA results, providing a small prediction error of 2.5±1.7 %. It allows a rapid analysis of structural parameters and design optimization. The fabricated mechanical amplifier could achieve an amplification ratio of $\times 8.44$ and axial displacement of 86 µm at a driving voltage of 100 V, respectively.

The new development of displacement amplifiers is a necessary effort that can lead to innovation in applications that perform precise manipulation and imaging in confined spaces. The proposed model was solely on deriving elastic deformation using Castigliano's theorem. Nevertheless, ongoing efforts include delving into stress concentration and conducting dynamic analysis to determine resonant frequencies in future studies. Furthermore, the implemented amplifier will be combined with a probe-based imaging system for depth-resolved imaging. This study will be crucial to developing a compact and compliant mechanism.

REFERENCES

[1] X. Gao, J. Yang, J. Wu, X. Xin, Z. Li, X. Yuan, X. Shen, and S. Dong, "Piezoelectric actuators and motors: materials, designs, and applications," *Adv. Mater. Technol.*, vol. 5, no. 1, p. 1900716, 2020.

[2] G. Y. Zhuang, H. W. Lee, and C. H. Liu, "Determination of the position and orientation of a flat piezoelectric micro-stage by moving the optical axis," *Rev. Sci. Instrum.*, vol. 85, no. 10, p. 105004, 2014.

[3] D. Koo, H. C. Park, P. L. Gehlbach, and C. Song, "Development and preliminary results of bimanual smart micro-surgical system using a ball-lens coupled oct distance sensor," *Biomed. Opt. Express*, vol. 7, no. 11, pp. 4816–4826, 2016.

[4] J. Im and C. Song, "Oblique injection depth correction by a two parallel oct sensor guided handheld smart injector," *Biomed. Opt. Express*, vol. 12, no. 2, pp. 926–939, 2021.

[5] J. Im, S. Park, and C. Song, "Handheld motorized injection system with fiber-optic distance sensors and adaptive time-delay controller," *Int. J. Optomechatronics*, vol. 18, no. 1, p. 2299023, 2024.

[6] A. Homayouni-Amlashi, M. Rakotondrabe, and A. Mohand-Ousaid, "Structural design and frequency tuning of piezoelectric energy harvesters based on topology optimization," in *IEEE ICRA*, 2023, pp. 5426–5432.

[7] N. Zhang, T. H. Tsai, O. O. Ahsen, K. Liang, H. C. Lee, P. Xue, X. Li, and J. G. Fujimoto, "Lissajous confocal fluorescent endomicroscopy with a lever mechanism and a frequency separation by an asymmetric polymer tube," *Opt. Lett.*, vol. 39, no. 2, pp. 186–188, 2014.

[8] J. Im, Y. Chang, M. H. Lee, D. Do, K. Lee, D. Gweon, and C. Song, "Lissajous confocal fluorescent endomicroscopy with a lever mechanism and a frequency separation by an asymmetric polymer tube," *International Journal of Optomechatronics*, vol. 17, no. 1, p. 2238009, 2023.

[9] J. Ueda, T. W. Secord, and H. H. Asada, "Large effective-strain piezoelectric actuators using nested cellular architecture with exponential strain amplification mechanisms," *IEEE/ASME Trans. Mechatronics*, vol. 15, no. 5, pp. 770–782, 2009.

[10] Q. Pan, Y. Liu, Y. Liu, L. Gong, L. He, and Z. Feng, "Design and fabrication of a large displacement piezoelectric actuator," in *2015 Symposium on Piezoelectricity, Acoustic Waves, and Device Applications (SPAWDA)*, 2015, pp. 261–264.

[11] Y. Hu, J. Ma, Y. Zhang, J. Li, Y. Hu, and J. Wen, "Performance comparison of two motion modes of a piezoelectric inertial linear motor and its potential application in cell manipulation," *Mech. Syst. Signal Process.*, vol. 157, p. 107743, 2021.

[12] J. Im, Y. Chang, and C. Song, "Modified phase-offset-driven lissajous scanning endomicroscopy with a polyimide-film-based frequency separator," *IEEE/ASME Trans. Mechatronics*, vol. 27, no. 6, pp. 4829–4839, 2022.

[13] J. Juuti, K. Kordás, R. Lonnakko, V. P. Moilanen, and S. Leppävuori, "Mechanically amplified large displacement piezoelectric actuators," *Sens. Actuator A Phys.*, vol. 120, no. 1, pp. 225–231, 2005.

[14] G. Lau, H. Lim, J. Teo, and Y. Chin, "Lightweight mechanical amplifiers for rolled dielectric elastomer actuators and their integration with bio-inspired wing flappers," *Smart Mater. Struct.*, vol. 23, no. 2, p. 025021, 2014.

[15] T. Schlinquer, A. Mohand-Ousaid, and M. Rakotondrabe, "Displacement amplifier mechanism for piezoelectric actuators design using simp topology optimization approach," in *IEEE ICRA*, 2018, pp. 4305–4311.

[16] S. Mohith, M. Rao, N. Karanth, S. M. Kulkarni, and A. Upadhya, "Development and assessment of large stroke piezo-hydraulic actuator for micro positioning applications," *Precis. Eng.*, vol. 67, pp. 324–338, 2021.

[17] L. Cao, "A new static and dynamic model for bridge-type displacement amplifier for use in piezoelectric actuators," in *2020 15th Symposium on Piezoelectrcity, Acoustic Waves and Device Applications (SPAWDA)*, 2021, pp. 460–464.

[18] S. B. Lavanya and G. R. Jayanth, "Optimal design of high bandwidth piezo-based nanopositioners employing bridge-type displacement amplifiers," in *2022 International Conference on Manipulation, Automation and Robotics at Small Scales (MARSS)*, 2022, pp. 1–6.

[19] H. Tang and Y. Li, "Optimal design of the lever displacement amplifiers for a flexure-based dual-mode motion stage," in *2012 IEEE/ASME International Conference on Advanced Intelligent Mechatronics (AIM)*, 2012, pp. 753–758.

[20] W. Dong, F. Chen, F. Gao, M. Yang, L. Sun, Z. Du, J. Tang, and D. Zhang, "Development and analysis of a bridge-lever-type displacement amplifier based on hybrid flexure hinges," *Precis. Eng.*, vol. 54, pp. 171–181, 2018.

[21] P. Schmitt and M. Hoffmann, "Engineering a compliant mechanical amplifier for mems sensor applications," *J. Microelectromech. Syst.*, vol. 29, no. 2, pp. 214–227, 2020.

[22] H. Tang, Y. Li, and X. Xiao, "A novel flexure-based dual-arm robotic system for high-throughput biomanipulations on micro-fluidic chip," in *IEEE ICRA*, 2013, pp. 1531–1536.

[23] G. Chen, Y. Ma, and J. Li, "A tensural displacement amplifier employing elliptic-arc flexure hinges," *Sensors and Actuators A: Physical*, vol. 247, pp. 307–315, 2016.

[24] Y. Zong, J. Liang, W. Pai, M. Ye, M. Ren, J. Zhao, Z. Tang, and J. Zhang, "A high-efficiency and high-precision automatic 3d scanning system for industrial parts based on a scanning path planning algorithm," *Opt. Lasers Eng.*, vol. 158, p. 107176, 2022.

[25] D. R. Rivera, C. M. Brown, D. G. Ouzounov, I. Pavlova, D. Kobat, W. W. Webb, and C. Xu, "Compact and flexible raster scanning multiphoton endoscope capable of imaging unstained tissue," *Proc. Natl. Acad. Sci. U.S.A.*, vol. 108, no. 43, pp. 17 598–17 603, 2011.

[26] M. B. Wallace and P. Fockens, "Probe-based confocal laser endomicroscopy," *Gastroenterology*, vol. 136, no. 5, pp. 1509–1513, 2009.

[27] Y. Chang, E. Z. Ahronovich, N. Simaan, and C. Song, "Exploring robot-assisted optical coherence elastography for surgical palpation," in *IEEE ICRA*, 2023, pp. 4768–4774.

[28] B. Qi, Z. Yu, Z. K. Varnamkhasti, Y. Zhou, and J. Sheng, "Toward a telescopic steerable robotic needle for minimally invasive tissue biopsy," *IEEE Robot. Autom. Lett.*, vol. 6, no. 2, pp. 1989–1996, 2021.

[29] V. L. Nguyen, "Design of an adjustable constant-force mechanism using a geared sarrus linkage and spring," *Mech. Mach. Theory*, vol. 189, p. 105417, 2023.

[30] G. Chen, S. Zhang, and G. Li, "Multistable behaviors of compliant sarrus mechanisms," *J. Mech. Robot.*, vol. 5, no. 2, p. 021005, 2013.

[31] Q. Zhang, J. Zhao, Y. Peng, H. Pu, and Y. Yang, "A novel amplification ratio model of a decoupled xy precision positioning stage combined with elastic beam theory and castigliano's second theorem considering the exact loading force," *Mech. Syst. Signal Process.*, vol. 136, p. 106473, 2020.

[32] M. M. Elsisy, M. H. Arafa, C. A. Saleh, and Y. H. Anis, "Modeling of a symmetric five-bar displacement amplification compliant mechanism for energy harvesting," *Sensors*, vol. 21, no. 4, p. 1095, 2021.

[33] Z. Xuan, T. Jin, N. S. Ha, N. S. Goo, T. H. Kim, B. W. Bae, H. S. Ko, and K. W. Yoon, "Performance of piezo-stacks for a piezoelectric hybrid actuator by experiments," *J. Intell. Mater. Syst. Struct.*, vol. 25, no. 18, pp. 2212–2220, 2014.

[34] M. Ling, J. Cao, M. Zeng, J. Lin, and D. J. Inman, "Enhanced mathematical modeling of the displacement amplification ratio for piezoelectric compliant mechanisms," *Smart Mater. Struct.*, vol. 25, no. 7, p. 075022, 2016.